MnO nanoparticles as the cause of ferromagnetism in bulk dilute Mn-doped ZnO

Diane Lançon, Gøran J. Nilsen, Andrew R. Wildes, Kirill Nemkovski, Ping Huang, Dóra Fejes, Henrik M. Rønnow, and Arnaud Magrez

Citation: Appl. Phys. Lett. **109**, 252405 (2016); doi: 10.1063/1.4972956
View online: http://dx.doi.org/10.1063/1.4972956
View Table of Contents: http://aip.scitation.org/toc/apl/109/25
Published by the American Institute of Physics

MnO nanoparticles as the cause of ferromagnetism in bulk dilute Mn-doped ZnO

Diane Lançon,[1,2] Gøran J. Nilsen,[3] Andrew R. Wildes,[2] Kirill Nemkovski,[4] Ping Huang,[1] Dóra Fejes,[5] Henrik M. Rønnow,[1] and Arnaud Magrez[5]
[1]*Laboratory for Quantum Magnetism, Institute of Physics, Ecole Polytechnique Federale de Lausanne (EPFL), CH-1015 Lausanne, Switzerland*
[2]*Institut Laue-Langevin, 71 Avenue des Martyrs, Grenoble 38000, France*
[3]*ISIS Facility, STFC Rutherford Appleton Laboratory, Didcot OX11 0QX, United Kingdom*
[4]*Jülich Centre for Neutron Science at Heinz Maier-Leibnitz Zentrum (MLZ) Forschungszentrum Julich GmbH, Lichtenbergstraße 1, 85748 Garching, Germany*
[5]*Crystal Growth Facility, Institute of Physics, Ecole Polytechnique Federale de Lausanne (EPFL), CH-1015 Lausanne, Switzerland*

(Received 14 October 2016; accepted 6 December 2016; published online 22 December 2016)

We show that the observed ferromagnetic behavior of ZnO lightly doped with Mn coincides with the presence of MnO nanoparticles, whereas cluster-free Mn doped ZnO behaves paramagnetically. This conclusion is reached by a study of the structural and magnetic properties of powdered samples of $(Mn_x,Zn_{1-x})O$ with $x \leq 0.033$ using polarized neutron scattering. Two types of samples were synthesized via, respectively, a solid state method and the decomposition of hydrozincite. Further characterization has been performed using standard X-ray diffraction and magnetization measurements. The results show evidence for the formation of MnO nanoparticles in the highest doped samples for both synthesis methods, with a ferromagnetic behavior attributed to uncompensated Mn^{2+} in the MnO nanoparticles. The lower Mn-doped samples showed no evidence for structural segregation or magnetic correlations and showed only a paramagnetic behaviour. *Published by AIP Publishing*. [http://dx.doi.org/10.1063/1.4972956]

Dilute magnetic semiconductor (DMS) oxides, and in particular, ZnO-DMS, have attracted a considerable attention since the experimental finding of room-temperature ferromagnetism in Mn^{2+} doped ZnO,[1] followed by the theoretical prediction of high temperature ferromagnetism in a wider range of dilute magnetic oxides and nitrides.[2] This prediction included a rich magnetic phase diagram as a function of the bound polaron overlap $\gamma^3\delta$ and the dopant concentration x, containing both insulating and metallic ferromagnetic, antiferromagnetic, and spin glass phases. Transition metal doped ZnO were suggested to be promising hosts for room-temperature ferromagnetism, due to the large bound polaron radius expected, for which the phase diagram predicts a transition from a spin glass phase to the metallic feromagnetic phase by increasing the dopant concentration.

The interest in room-temperature ferromagnetism in ZnO-DMS is largely due to its strong potential impact on developing tools for spintronics. However, the experimental results showing room-temperature ferromagnetism results have been disputed. An abundance of contradicting views on ZnO-DMS has arisen, with ferromagnetism found in some Mn and Co doped ZnO studies,[3] and not in others[4] (for a review of reported results, see Ref. 5). The main question in all of these cases concerns the nature of ferromagnetism in transition metal-doped zinc oxide[6–8] and whether the ferromagnetic signatures depend on the fabrication method.[9] Indeed, in the context of potential spintronics applications, it is crucial to distinguish whether the ferromagnetic properties come from a homogenous distribution of the transition-metal ion, or from a segregated phase within the semi-conducting matrix.[8] In addition, the experimental difficulty of the detection of a non-homogeneous spin distribution further complicates the debate.[10]

The most commonly used probe to detect the presence or absence of clustering, phases and impurities in the samples is the X-ray diffraction[1,3,11] (XRD). For this purpose, however, elemental contrast between Mn and Zn is poor. In this article, we attempt to clarify the question of the nature of ferromagnetism in Mn doped ZnO by using polarised neutron scattering, which is a powerful technique for distinguishing between short-ranged and long-ranged order. These results are combined with standard XRD measurements and magnetisation measurements in order to explain the discrepancies between previous studies.

Powdered $Zn_{1-x}Mn_xO$ samples were prepared using two synthesis methods, a conventional solid state method and a soft chemistry route. In the first method, Mn-doped ZnO was synthesized by the solid state reaction from Mn carbonate and Zn oxide. A stoichiometric mixture of Mn carbonate and Zn oxide was ground in acetone and annealed in an $8\%H_2$ in N_2 atmosphere at 400 °C. The composition of the sample was measured by an energy dispersive X-ray spectroscopy (EDX), and the Mn doping was estimated to be $x = 2\%$. The second synthesis method involved decomposition of the Mn-doped zinc carbonate produced by the hydrothermal treatment of an aqueous solution of Mn nitrate, Zn nitrate, and urea, similarly to Mickovic *et al.*[12] The obtained Mn-doped Zn carbonate was then decomposed into Mn doped ZnO by heat treatment at 400 °C in a forming gas ($8\%H_2$ in N_2), introducing oxygen vacancies[13,14] to have a larger δ parameter. The actual concentration of Mn in the ZnO materials was measured by X-Ray fluorescence (XRF) with a 30 μm size

TABLE I. List of growth method and Mn^{2+} concentration for each sample, with the reference code.

Code	Growth method	Mn^{2+} doping %
S_2	solid state	~2
$H_{3.28}$	decomposition of hydrozincite	3.28 ± 0.02
$H_{1.57}$	decomposition of hydrozincite	1.57 ± 0.02
$H_{1.14}$	decomposition of hydrozincite	1.14 ± 0.01
$H_{0.59}$	decomposition of hydrozincite	0.59 ± 0.01
ZnO	from supplier	0

probe. Table I summarizes the result of these measurements. As the hydrozincite decomposition proceeds at a low temperature, the homogeneity of the transition metal's distribution in the hydrozincite matrix is preserved, provided the concentration of the transition metal is lower than its solubility in ZnO. No gradient in the Zn distribution could be seen in the XRF measurements, as such the samples were thought to be homogenous. Finally, a pure ZnO sample, for which no magnetic scattering is expected, was used as a control. Table I shows a summary of the samples with their corresponding Mn^{2+} concentrations and an abbreviation that will be used throughout the article.

The DC magnetic susceptibility of each sample was measured using a Superconducting QUantum Interference Device (SQUID) magnetometer (Quantum Design MPMS). The magnetisation as a function of field was measured at 5 K using a conventional hysteresis field sweep between ± 5 T. XRD measurements were carried out on an Empyrean diffractometer (Panalytical). The diffraction patterns were measured with Cu K_α radiation ($\lambda = 1.54$ Å).

The polarized neutron experiments were performed on two diffractometers: D7 at the Institut Laue Langevin (ILL),[15] France and DNS at the Forshungsreactor Munchen II (FRMII),[16,17] Germany. The working principle was similar for both: a guide field sets the polarisation axis for the neutron beam, and then one of the spin states was selected by reflection from a supermirror bender. This was followed by a Mezei-type precession coil neutron spin flipper, which flipped the spin with respect to the guide field direction. The flipper was switched on or off depending on whether processes flipping the neutron spin or not were being measured. A set of coils around the sample position rotated the polarization into one of three orthogonal directions for XYZ polarization analysis,[18] and the outgoing polarization was analyzed by another set of supermirror benders. A total of six cross sections were collected: spin flip and non-spin flip for each field orientation at the sample position. The different contributions to the scattering cross section (magnetic, spin incoherent and nuclear and isotope incoherent) were then separated by a linear combination of these cross sections (see Ref. 15 for details). The data were reduced according to the standard procedure on D7, with a characterisation of the polarizing efficiency of the instrument using scattering from amorphous quartz and of the detector efficiency using scattering from vanadium. The background was estimated using measurements of an empty can and a can containing cadmium, weighted by the transmission of the sample. The absolute cross section per solid angle and the formula unit of Mn:ZnO (barns sr^{-1} f.u.$^{-1}$) was obtained by calibration with vanadium. On DNS, the incident wavelength was 4.13 Å, while the two incident wavelengths used on D7 were: $\lambda = 3.1$ and 4.8 Å. The samples all weighed ~10 g and were loaded in aluminium cans of 60 mm height and either 15 mm or 20 mm diameter (on DNS and D7, respectively).

Fig. 1 shows the XRD measurements of the Mn^{2+} doped samples around respectively $Q = 2.83$ Å^{-1} and $Q = 4$ Å^{-1}, corresponding to expected positions for the (200) and (220) Bragg peaks of MnO. The presence of MnO is clearly observed in S_2, the sample grown by the solid state method. In $H_{3.28}$, there may be an indication of the presence of MnO at the scattering angle corresponding to (200) with a very broad signal, but no peak appears at the expected Q position for the (220) Bragg peak. For the rest of the samples ($H_{1.57}$, $H_{1.14}$, and $H_{0.59}$), there is no indication of the presence of MnO.

Fig. 2 presents the results of the SQUID magnetisation measurements as a function of magnetic field at 5 K. The magnetisation of S_2 in Fig. 2(a) shows a clear hysteresis from which a 6480 Oe coercive field can be deduced. Similarly, a smaller hysteresis can be observed in Fig. 2(b) for $H_{3.28}$, with an estimated coercive field of 301 Oe. Very close examination of the magnetisation for the lower dopings: $H_{1.57}$, $H_{1.14}$, and $H_{0.59}$, are shown in the insets of Figs. 2(c)–2(e), shows no clear hysteresis, with an upper limit on the coercive field of 19, 10, and 5 Oe for $H_{1.57}$, $H_{1.14}$, and $H_{0.59}$ respectively. This is consistent with the paramagnetic behavior, and these data were fitted with a Brillouin function for $S = 5/2$ and $g = 2$.

The polarised neutron data were analysed to separate the magnetic, nuclear, and spin incoherent cross sections, allowing a comparison of the samples with respect to the synthesis method and the Mn^{2+} doping level. Figure 3 shows the nuclear cross section for each sample, including the pure ZnO reference. The ZnO nuclear Bragg peaks are resolution-limited, and thus were used to obtain the instrumental resolution. We observe an upturn starting at Q lower than 0.7, which is possibly due to multiple scattering.

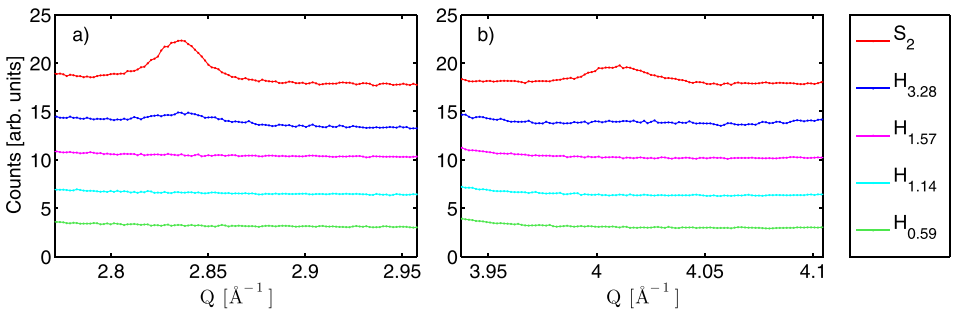

FIG. 1. X-Ray diffraction patterns for the five Mn^{2+} doped samples. a) Diffraction profile around $Q = 2.83$ Å^{-1}, which corresponds to the (2 0 0) Bragg peak position of MnO. b) Diffraction profile around $Q = 4$ Å^{-1}, corresponding to the (2 2 0) Bragg peak position of MnO.

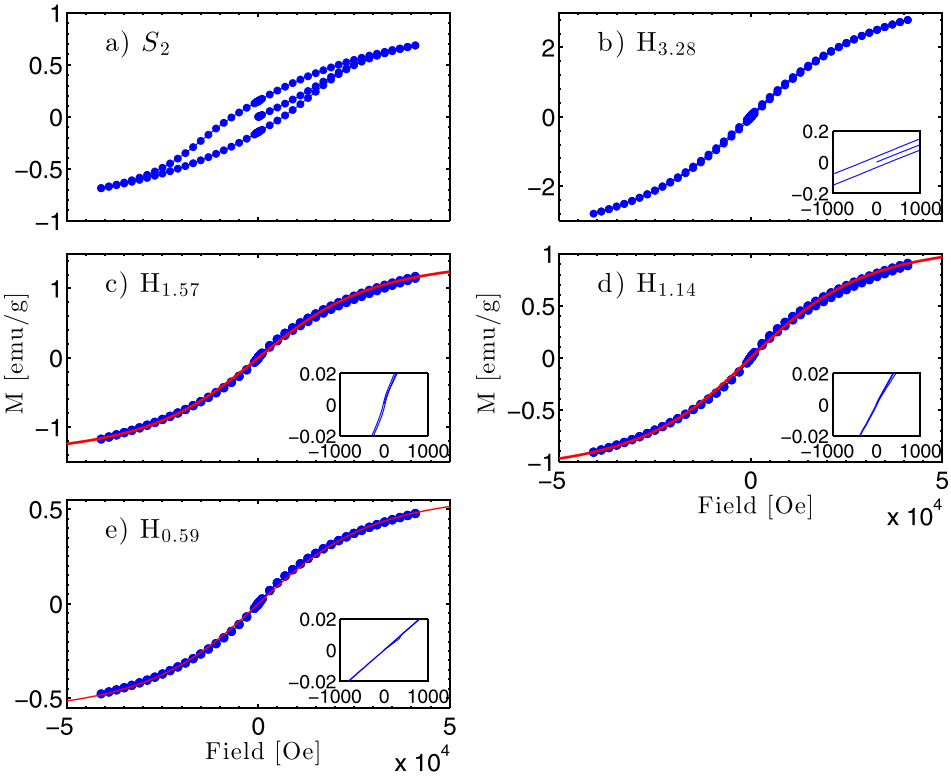

FIG. 2. Magnetisation as a function of field at 5 K. Panel *a* corresponds to the solid state method sample S_2, while panels *b-e* concerns the decomposition of hydrozincite samples $H_{3.28}$, $H_{1.57}$, $H_{1.14}$, and $H_{0.59}$. Calculated Brillouin function for $S = 5/2$ is shown in red for panels *c-e*. Insets show the region around $H = 0$; only S_2 (a) and $H_{3.28}$ (b) show any hysteresis.

The strong Bragg peaks at $Q = 2.23$, 2.43, and 2.54 Å^{-1} correspond respectively to the ZnO nuclear structure peaks (1 0 0), (0 0 2), and (1 0 1). The inset shows a zoom of the nuclear and isotope incoherent scattering away from the Bragg peaks, which contains both diffuse scattering from substitutional disorder as well as small peaks not expected from the ZnO structure. Sample $H_{0.54}$ features weak peaks at $Q = 1.25$ and 1.95 Å^{-1} while sample $H_{1.14}$ and $H_{1.57}$ have the same weak peaks at $Q = 1.25$ and 1.95 Å^{-1} and an additional sharper peak at 1.73 Å^{-1}. These could be due to impurity phase, although they cannot be indexed using any of the most common Mn-based and Zn-based impurities. However, we do not anticipate these peaks to have any effect of magnetism. In addition, the inset of the low Q scattering data shows that sample H_{328} has the strongest nuclear diffuse scattering cross-section, followed by $H_{1.57}$ and $H_{1.14}$ with very similar cross sections, and then $H_{0.54}$. Finally, S_2 shows the lowest cross sections, which is equivalent to the scattering of the pure ZnO sample. The magnitudes of diffuse scattering are evidence that the hydrozincite samples do have a site disorder, while the solid state sample has very little diffuse scattering, which is consistent with separate phases. In addition, no clear features corresponding to nuclear short range order were observed in the nuclear cross-section.

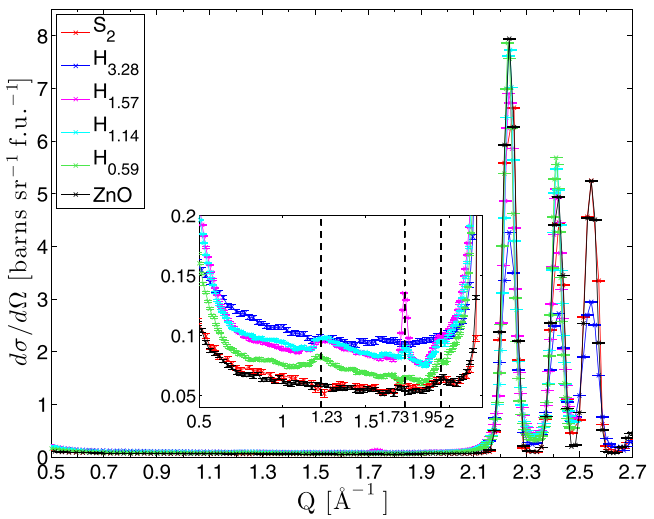

FIG. 3. Nuclear and isotope incoherent cross section for all the samples. The strong Bragg peaks at $Q = 2.23$, 2.43, and 2.54 Å^{-1} correspond to ZnO nuclear structure peaks. The inset is a zoom on the low Q scattering, showing very weak Bragg peaks probably corresponding to impurity phases.

The magnetic cross sections are presented in Fig. 4. Panels *a* and *b* of Fig.4 shows that the magnetic cross sections of S_2 and $H_{3.28}$ have clear features at $Q \sim 1.24$ Å^{-1}, which is the expected Q position for the $\left(\frac{1}{2}\frac{1}{2}\frac{1}{2}\right)$ MnO Bragg peak. These features are broader than the structural Bragg peaks, and reflect a segregation of MnO inside ZnO with a distribution of particle size and shape that cannot be established exactly. To estimate this, the data were fitted using two Voigt functions, assuming a Gaussian resolution extracted from the nuclear peak widths, and a Lorenzian broadening. One results in a narrow and more intense peak at $Q = 1.24$ Å^{-1}, corresponding exactly to the $|Q|$ for the $\left(\frac{1}{2}\frac{1}{2}\frac{1}{2}\right)$ peak of MnO, while the second gives a smaller and broader peak around $Q = 1.48$ Å^{-1}. This type of scattering has been observed previously in studies of MnO nanoparticles[19] with a particle size distribution average of 100 Å. A rough estimation of the correlation length of the nanoparticles observed in S_2 are 43 ± 5 and 14 ± 4 Å while they are of 16.7 ± 3 and 4.8 ± 0.7 Å for $H_{3.28}$. By comparing the integrated peak intensity of the (1 0 0) ZnO nuclear Bragg peak with the total integrated MnO magnetic Bragg intensities, the volume fraction of MnO nanoparticles in the ZnO matrix has been calculated to be 0.83% for $H_{3.28}$ and 0.25% for S_2.

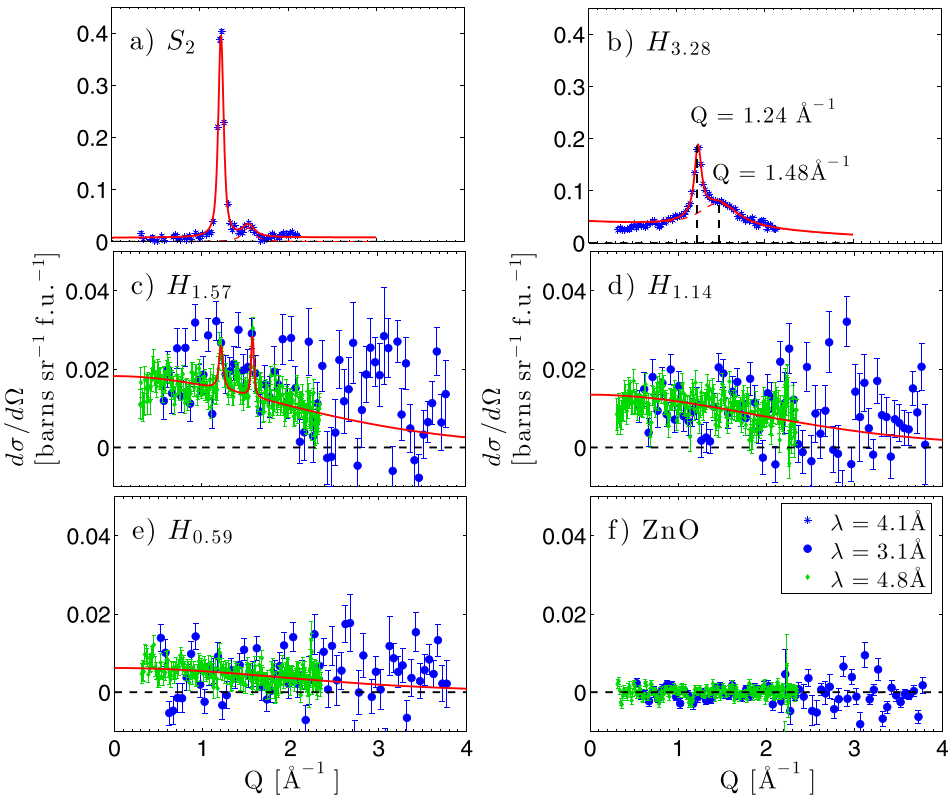

FIG. 4. Magnetic cross section. Blue stars correspond to $\lambda = 4.1$ Å (DNS), blue circles to $\lambda = 3.1$ Å (D7), and green diamonds to $\lambda = 4.8$ Å (D7). Panel a shows the solid state method sample, while panels b-e concern the decomposition of hydrozincite samples. Pure ZnO is shown in panel f. The solid red line is a fit with Voigt functions for the magnetic peaks, and the Mn^{2+} forms factor for the paramagnetic background.

The analysis of the magnetic scattering cross section for S_2 and $H_{3.28}$ shows clearly the presence of segregated MnO in the ZnO matrix. In addition, a clear ferromagnetic behavior was observed in the magnetisation measurements (Fig. 2). It is therefore likely that ferromagnetism in these samples comes from uncompensated surface spins on the MnO nanoparticles, which has been observed in other studies.[19,20]

At 1.57% Mn^{2+} doping (Figure 4(c)), very weak and narrow peaks are again observed at the same Q position. Their intensity relative to the background is much lower than for the higher doping, and would correspond to a MnO volume fraction in ZnO matrices of 0.06%. These peaks disappear by 50 K, well below $T_N \sim 122$ K for MnO, and their peak width is smaller than the resolution, hence they may be an artifact of the measurement, although the presence of a small amount of bulk MnO cannot be excluded.

For Mn^{2+} dopings of 1.57% and below (Figs. 4(c)–4(e)), the spectrum is dominated by diffuse form-factor-like scattering, as expected for paramagnetic behavior. The cross section of the more lightly doped samples $H_{1.14}$ and $H_{0.59}$ show only paramagnetic behavior in the measured Q range, and were fitted with the Mn^{2+} form factor. Fig. 4(f) shows the magnetic cross section for the pure ZnO sample, which is zero as expected, providing a baseline for the other measurements.

Within the assumption of paramagnetic behavior, the $Q = 0$ amplitude of the magnetic cross section $\frac{d\sigma}{dQ}(Q=0)$ can be used to calculate the effective moment μ_{eff} from the spin-only equation for the magnetic cross section:[21] $\frac{d\sigma}{dQ} = \frac{2}{3}\left(\frac{\gamma r_0}{2}\right)^2 N g^2 F^2(Q) S(S+1)$. Mn^{2+} has $3d^5$ orbitals and assumes a high-spin state with $S = \frac{5}{2}$. Taking into account the Mn^{2+} concentration, Table II shows the Mn^{2+} effective moment μ_{eff} obtained from the form-factor fits of the lightly doped samples. Broadly speaking, the values are close to the expected $\mu_{eff} = \sqrt{g^2 S(S+1)} = 5.92\mu_B$ for Mn^{2+}.

Previous experimental results had placed Mn:ZnO in the ferromagnetic phase of the magnetic phase diagram of the theoretical prediction mentioned in the introduction[2] for doping of 2.2% and for temperatures up to room temperature. This theory suggests that the room temperature ferromagnetism and other magnetic phase in DMS are caused by the coexistence of defects and dopant cation at small doping. The band created by the defects hybridizes with the d orbital of the dopant, and the spin are polarised via Hund's exchange.

However, from these polarised neutron scattering results, we do not observe any spin glass or ferromagnetic phase in Mn:ZnO, which implies that either the defect concentration is too low, that the polaron radius is not sufficiently large, or that the bands are not close enough to hybridize. In that context, we thus conclude that Mn:ZnO is restricted to the paramagnetic region of the phase diagram for all cluster-free doping percentages even at 2 K, at least in the case of these synthesis methods.

While magnetisation measurements show clear evidence for ferromagnetism in S_2, the 2% doped sample grown by the solid state method, neutron polarisation analysis, and XRD measurements confirm that there is segregation of manganese into MnO and MnO nanoparticles. On the other

TABLE II. Effective moment of Mn^{2+} obtained from the $Q = 0$ intercept of the magnetic cross sections.

Mn^{2+} doping [%]	Estimated μ_{eff} [μ_B/atom]	$Q = 0$ intercept
1.57	4.87 ± 0.05	$1.82 \cdot 10^{-2} \pm 3.10^{-4}$
1.14	4.91 ± 0.05	$1.35 \cdot 10^{-2} \pm 3.10^{-4}$
0.59	4.62 ± 0.28	$6.18 \cdot 10^{-3} \pm 7.10^{-4}$

hand, XRD does not clearly show the presence of MnO in $H_{3.28}$, but the neutron scattering data demonstrate that the ferromagnetism appearing in the magnetisation measurements is strongly linked to the formation of MnO nanoparticles. Size estimates of the nanoparticles could also be obtained from fits of the polarised neutron data and are typically 20–50 Å. Lower Mn^{2+} doping result in paramagnetism with no indication of ferromagnetic short-range order, neither in polarised neutron scattering nor in magnetisation measurements. This leads to the conclusion that ferromagnetic correlations in these Mn^{2+} doped ZnO samples do not come from substitution of the zinc by manganese in the ZnO matrix. Instead, MnO nanoparticles form and the ferromagnetism most likely comes from unpaired spins at the nanoparticle boundaries. Polarised neutron scattering has proved to be extremely sensitive to spin correlation and clustering in these compounds.

The authors wish to thank the Institut Laue-Langevin and FRMII for the use of their neutron instrumentation, and particularly the instrumental team of D7 and DNS. The work was supported by the Swiss National Science Foundation, and its sinergia network MPBH.

[1]P. Sharma, A. Gupta, K. V. Rao, F. J. Owens, R. Sharma, R. Ahuja, J. M. O. Guillen, B. Johansson, and G. A. Gehring, Nat. Mater. **2**, 673–677 (2003).
[2]J. M. D. Coey, M. Venkatesan, and C. B. Fitzgerald, Nat. Mater. **4**, 173–179 (2005).
[3]Y. Q. Chang, D. B. Wang, X. H. Luo, X. Y. Xu, X. H. Chen, L. Li, C. P. Chen, R. M. Wang, J. Xu, and D. P. Yu, Appl. Phys. Lett. **83**, 4020–4022 (2003).
[4]G. Lawes, A. S. Risbud, A. P. Ramirez, and R. Seshadri, Phys. Rev. B **71**, 045201 (2005).
[5]S. J. Pearton, W. H. Heo, M. Ivill, D. P. Norton, and T. Steiner, Semicond. Sci. Technol. **19**, R59 (2004).
[6]K. R. Kittilstved, W. K. Liu, and D. R. Gamelin, Nat. Mater. **5**, 291–297 (2006).
[7]T. Dietl, H. Ohno, F. Matsukura, J. Cibert, and D. Ferrand, Science **287**, 1019–1022 (2000).
[8]J. L. Costa-Krämer, F. Briones, J. F. Fernandez, A. C. Caballero, M. Villegas, M. Diaz, M. A. García, and A. Hernando, Nanotechnology **16**, 214 (2005).
[9]H.-J. Lee, S.-Y. Jeong, C. R. Cho, and C. H. Park, Appl. Phys. Lett. **81**, 4020–4022 (2002).
[10]T. Dietl, Nat. Mater. **9**, 965–974 (2010).
[11]X. L. Wang, K. H. Lai, and A. Ruotolo, J. Alloys Compd. **542**, 147–150 (2012).
[12]Z. Micković, A. Duncan, A. Sienkiewicz, M. Mionić, L. Forró, and A. Magrez, Cryst. Growth Des. **10**, 4437–4441 (2010).
[13]B. Du Ahn, S. H. Oh, C. H. Lee, G. H. Kim, H. J. Kim, and S. Y. Lee, J. Cryst. Growth **309**, 128–133 (2007).
[14]J. S. Kang, H. S. Kang, S. S. Pang, E. S. Shim, and S. Y. Lee, Thin Solid Films **443**, 5–8 (2003).
[15]J. Stewart, P. Deen, K. Andersen, H. Schober, J.-F. Barthélémy, J. Hillier, A. Murani, T. Hayes, and B. Lindenau, J. Appl. Crystallogr. **42**, 69–84 (2009).
[16]W. Schweika and P. Böni, Physica B **297**, 155–159 (2001).
[17]Heinz Maier-Leibnitz Zentrum *et al*. (2015), DNS: Diffuse scattering neutron time-of-flight spectrometer. Journal of large-scale research facilities **1**, A27.
[18]O. Schärpf and H. Capellmann, Phys. Status Solidi A: Appl. Res. **135**, 359–379 (1993).
[19]T. Chatterji, Y. Su, G. N. Iles, Y.-C. Lee, A. P. Khandhar, and K. M. Krishnan, J. Magn. Magn. Mater **322**, 3333–3336 (2010).
[20]C.-C. Lin, C.-J. Chen, and R.-K. Chiang, J. Crystal Growth **338**, 152–156 (2012).
[21]G. L. Squires, *Introduction to the Theory of Thermal Neutron Scattering* (Cambridge University Press, 2012).